

Design and evaluation of an integrated scanning laser triangulation sensor

Johannes Schlarp, Ernst Csencsics and Georg Schitter

Christian Doppler Laboratory for Precision Engineering for Automated In-Line Metrology at the Automation and Control Institute, Technische Universität Wien, Vienna A-1040, Austria

ARTICLE INFO

Keywords:

Optical Sensing and Sensors
3D Sensor
Laser Sensor
Fast Steering Mirror
System Analysis and Design

ABSTRACT

This work presents the design, simulation, control and experimental result of an optical scanning laser sensor for 3D imaging. The system design satisfies the Scheimpflug condition even though only the illumination path is scanned by a compact fast steering mirror (FSM). To reconstruct the surface profile from measured quantities and model parameters, geometrical relations are used. The influence of a misalignment on the achievable resolution is determined, using ray-tracing simulations. To scan the area of interest an adapted scan trajectory is employed, such that a uniform spatial resolution is generated. The system captures the sample with 100 x 100 pixels and achieves a framerate of 10 s. The lateral scan area of 15 x 23 mm is obtained with a maximum lateral resolution of 60 μm . Through the optical scan the measurement time can be reduced by a factor of 400 compared to a mechanical scanning triangulation sensor system.

1. Introduction

For production of the future, fast and high resolution three dimensional (3D) in-line metrology systems are required, since the number of produced goods is constantly increasing [1, 2, 3]. In addition in-line metrology enables to optimize the manufacturing process and machine tools settings [4], such that the number of defective goods can be reduced [5]. State of the art 3D measurement systems are mechanical scanning systems, like coordinate measurement machines [6]. These systems manipulate the position of the sample or sensor, e.g. a tactile probe or an optical point sensor, with external actuators [7]. The achievable scan speed of such a mechanical scanning system is strongly restrained by the large moving mass [8]. If a higher throughput is required, camera-based systems, e.g. based on structured light, are typically applied [9]. The maximum achievable resolution of these systems is about 10 μm and strongly depends on the measurement range [10]. For example the achievable depth resolution of Kinect 1 sensor increases quadratically with the distance, such that a depth resolution of a few millimeter is achieved at the start of the measurement range (0.5 m), which increases to 70 mm towards the end of the measurement range (5 m) [11]. This measurement principle is, however, strongly sensitive to reflective properties of the sample and external illumination [12].

Optically scanned point sensors, e.g. laser triangulation sensors, can overcome this limitations, since illumination intensity is adjusted to the sample and optical filters reduce influence of external illumination [10]. Due to their large measurement range of up to 1 m and high resolution of down to 30 nm, triangulation sensors are one of the most commonly used optical sensors for quality control tasks [13]. As with camera-based systems, the achievable resolution decreases

with the obtainable measurement area.

The main components of these sensors are a laser source, an imaging lens and a detector [14]. In order to precisely obtain the distance between sample and sensor, the diffusely scattered laser light spot from the sample must be projected sharply onto the detector [10]. To project an object in the object plane sharply onto the image plane, as illustrated in Fig. 1(a), the thin-lens equation must be satisfied, which can be given by

$$\frac{1}{f} = \frac{1}{a} + \frac{1}{a'}, \quad (1)$$

with the focal length of the lens f , the distance between lens and object plane a and the distance between lens and image plane a' . The thin-lens equation is, however, only valid, if all three planes are parallel, which is not the case for the components of a triangulation sensor. In order to generate

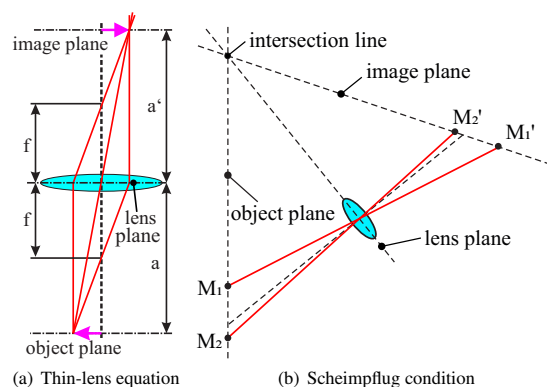


Figure 1: Schematic illustration of (a) the thin-lens equation and (b) the Scheimpflug condition, as generalized form for tilted planes.

schlarp@acin.tuwien.ac.at (J. Schlarp)
www.acin.tuwien.ac.at/en/ (J. Schlarp)
ORCID(s): 0000-0002-1157-5462 (J. Schlarp)

Design and evaluation of an integrated scanning laser triangulation sensor

a sharp projection, the components of the triangulation sensor are aligned according to the Scheimpflug condition [15], which is a generalized form of the thin-lens equation for non parallel planes. The Scheimpflug condition is fulfilled, if the object, lens and image plane intersect in a single line (intersection line), as depicted in Fig. 1(b).

In [16] two optical scanning systems are presented, which manipulate only the optical path of a line sensor by a fast steering mirror (FSM). Since the moving mass of an integrated compact optical scanning system can be significantly smaller as compared to external mechanical scanning systems, higher scan speeds can be achieved, without impairing lateral resolution of the measurement system [17]. The first system design, presented in [16], manipulates both optical paths of the sensor (see Fig. 2(a)), such that the basic measurement geometry of the sensor is not affected and the Scheimpflug condition is maintained. In the second system design only the illumination path of the sensor is scanned (see Fig. 2(b)), such that an FSM with a smaller aperture size can be used, which enables an even higher scan speed. Furthermore, the FSM can generally be positioned closer to the sensor, such that a larger lateral scan range is enabled as compared to the system design which manipulates both optical paths. However, the system design violates the Scheimpflug condition, such that an additional measurement error is introduced [18].

The contribution of this paper is (a) design of an integrated optical scanning sensor system, which manipulates only the illumination path of the sensor, while maintaining the Scheimpflug condition, (b) image reconstruction from the measured quantities with geometrical relations, (c) analysis of the influence of misalignment on the lateral resolution, and (d) validation of the system performance. This paper is an extension of contribution [19] and provides a deeper insight in system design, image reconstruction, effects of misalignment and applied scan trajectory. The aim of the paper is the development of an optical scanning point triangulation sensor, achieving a high scan speed, suitable for in-line metrology. In Section 2 the system design is presented and quantified using ray-tracing simulations. Section 3 provides a system overview, describes geometrical relations for image reconstruction and investigates the effects of a misalignment. The experimental setup, controller design and scan trajectory are described in Section 4. Section 5 presents measurement results and determines system performance. Finally, Section 6 concludes the paper and presents a brief outlook.

2. Scanning Triangulation Sensor Design

Ray-tracing simulations are used to investigate the obtainable lateral scan range, the influence of alignment errors, as well as aberrations of the optical system in advance. For the simulation, the orientation, position and optical parameters, e.g. focal length, of the used components are initially defined. Based on these settings, the simulation program (type: Matlab, Mathworks, USA) calculates the resulting optical path.

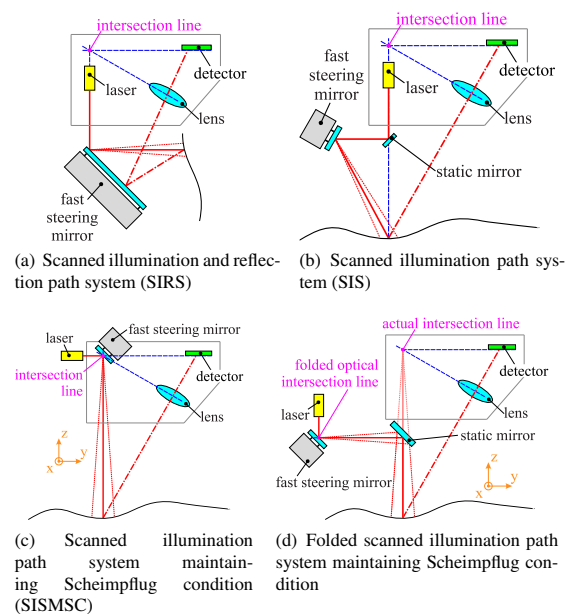


Figure 2: System designs which manipulate the optical path of a laser sensor. (a,b) show previously reported designs [16]. (c) depicts a design which satisfies the Scheimpflug condition, while (d) shows the proposed design, which folds the optical path of (c) by a static mirror.

As described earlier, a scanned illumination path system (SIS) was proposed in [16]. The schematic of this system design is shown in Fig. 2(b) and consists of a laser line sensor, a static mirror and an FSM. The static mirror is used to redirect the optical beam, which is generated by a laser module inside the sensor, onto the center of the aperture of the FSM. The orientation of the FSM is selected such that the laser beam intersects with the primary unmodified illumination path of the sensors in the mid measurement range (see Fig. 2(b)), which maximizes the resulting lateral scan area.

The calculated lateral scan area of the SIS, is shown in Fig. 3(a), for various distances between sensor and sample. As can be observed, not only the size of the achievable lateral scan area changes over distance, but also the center, such that the lateral scan area at the start of the measurement range can not be captured over the entire measurement range. Furthermore, the field of view of the imaging system inside the laser triangulation sensor is generally limited, such that conceivably the complete lateral scan area can not be captured by the sensor at the start and end of the measurement range.

To observe the same scan area at the start and end of the measurement range, the incident laser beam needs to be parallel to the object plane. The observable lateral scan area is maximized, if the laser beam is congruent with the object plane, since the field of view of the imaging system is designed to capture the object plane. As discussed in Sec-

Design and evaluation of an integrated scanning laser triangulation sensor

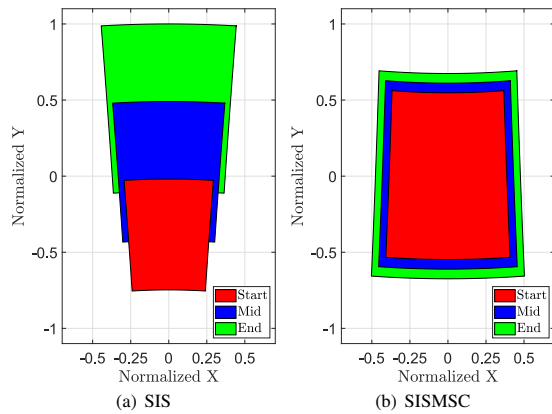


Figure 3: Simulated lateral scan area of both system designs at the start, mid and end of the measurement range. The center of the scan area changes over the distance for the SIS.

tion 1, a sharp projection of the scattered laser spot on the sample onto the detector is necessary, to precisely determine the distance between sensor and sample. For point or line triangulation sensors this can be realized by aligning the object, lens and image plane according to the Scheimpflug condition. For a three dimensional measurement system, however, the position and orientation of the object plane changes during the scanning motion, such that it is difficult to fulfil the Scheimpflug condition. By placing the mirror surface of the FSM on the intersection line of the lens and image plane the condition can be satisfied at each measurement point [20], since the object plane rotates around the intersection line. The schematic setup of this scanned illumination path system maintaining the Scheimpflug condition (SISMSC) is shown in Fig. 2(c). Figure 3(b) depicts the calculated lateral scan area of the SISMSC. As can be observed, the scan area only expands towards larger distances, such that the scan area at the start of the measurement range can be captured over the entire measurement range.

3. System Description and Image reconstruction

3.1. System Description

A laser line sensor (type: LLT 2810-25, Micro-Epsilon GmbH, Germany) with a measurement range of 25 mm and resolution of $10 \mu\text{m}$ is selected as starting point for the scanning system. From the sensor only the lens set, detector and evaluation unit are used. The surface of the sample is illuminated by a laser beam, which is generated from a dot laser module. To change position of the laser spot on the sample, the orientation of the laser beam is manipulated by means of an FSM. For the used laser line sensor, the intersection line is too close to the circuit board of the evaluation unit, such that the FSM surface cannot be positioned directly on the actual intersection line, as described in Section 2. By insert-

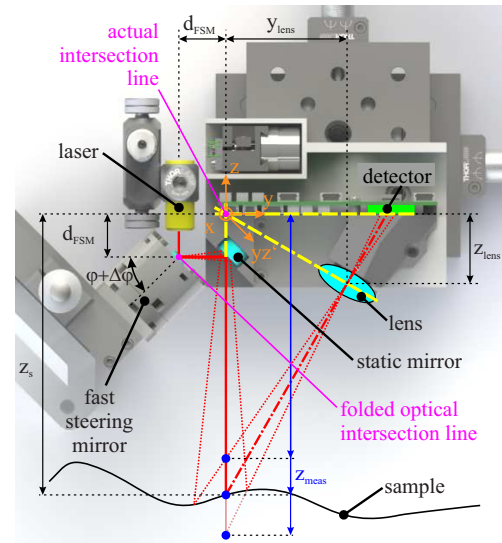


Figure 4: Schematic setup of the scanning triangulation system with characteristic dimensions. The position of the laser spot on the sample can be manipulated by the FSM. Through the static mirror, the FSM is optically positioned on the intersection line.

ing an additional static mirror between the FSM and sample, as depicted in Fig. 2(d), the optical path between the static mirror and laser source can be folded around the surface of the static mirror, such that the FSM is optically placed on the intersection line. As can be observed in Fig. 4, the distance d_{FSM} between FSM and static mirror has to be equal to the distance between static mirror and intersection line. This distance together with the angular range of the FSM determines the required aperture size of the static mirror.

To manipulate the illumination path a novel high performance compact FSM is used [21]. The system dimensions are as small as $\varnothing 32 \times 30 \text{ mm}$. The orientation of the FSM φ and static mirror is 45° with respect to the xz -plane, to enable good alignment of the system components. The outer diameter of the compact FSM is 32 mm, such that the distance d_{FSM} is selected to 20 mm. At this distance a static mirror (type: PF05-03-P01, Thorlabs Inc., USA) with an aperture size of 12.7 mm is sufficient to redirect the laser beam to the sample over the entire scan range.

3.2. Image Reconstruction

The measured quantities consist of $\Delta\varphi$, $\Delta\theta$, which are the angular positions of the FSM around the x -, yz' -axis, and z_{meas} , which is the distance measured by the laser line sensor. As can be observed in Fig. 4, the distance z_{meas} measured by the sensor is acquired in the xz -plane, such that the reconstructed distance only corresponds to the distance between sensor and sample z_s at $y = 0 \text{ mm}$. To reconstruct the surface profile of the sample from the measured quantities, geometrical relations need to be determined.

Design and evaluation of an integrated scanning laser triangulation sensor

The lateral position of the laser spot on the sample can be calculated with vector arithmetic. The direction \mathbf{d}_L of the laser beam generated from the laser dot module can be given by

$$\mathbf{d}_L = \begin{bmatrix} 0 \\ 0 \\ -1 \end{bmatrix}. \quad (2)$$

The direction of a reflected laser beam \mathbf{d}_{RefI} can be calculated with the Housholder matrix [22] to

$$\mathbf{d}_{\text{RefI}} = (\mathbf{E} - 2\mathbf{n}_{\text{Mirr}}\mathbf{n}_{\text{Mirr}}^T) \mathbf{d}_{\text{Inc}}, \quad (3)$$

in which \mathbf{n}_{Mirr} describes the normal vector of the mirror and \mathbf{d}_{Inc} the direction of the incoming laser beam. The normal vector of the FSM can be described by the roll pitch yaw angles [23] in the following form

$$\mathbf{n}_{\text{FSM}} = \begin{bmatrix} 0 \\ 0 \\ 1 \end{bmatrix}^T \begin{bmatrix} 1 & 0 & 0 \\ 0 & c_{\varphi+\Delta\varphi} & -s_{\varphi+\Delta\varphi} \\ 0 & s_{\varphi+\Delta\varphi} & c_{\varphi+\Delta\varphi} \end{bmatrix} \begin{bmatrix} c_{\Delta\vartheta} & 0 & s_{\Delta\vartheta} \\ 0 & 1 & 0 \\ -s_{\Delta\vartheta} & 0 & c_{\Delta\vartheta} \end{bmatrix}, \quad (4)$$

with $c_i = \cos(i)$, $s_i = \sin(i)$, $\Delta\varphi$ and $\Delta\vartheta$ the angular position of the FSM around the x and yz' -axis, respectively. Solving this equation leads to

$$\mathbf{n}_{\text{FSM}} = \begin{bmatrix} -\cos(\varphi + \Delta\varphi) \sin(\Delta\vartheta) \\ \sin(\varphi + \Delta\varphi) \\ \cos(\varphi + \Delta\varphi) \cos(\Delta\vartheta) \end{bmatrix}. \quad (5)$$

The roll pitch yaw angles can also be used to determine the normal vector of the static mirror, which can be given by

$$\mathbf{n}_{\text{SM}} = \begin{bmatrix} 0 \\ -\sqrt{2} \\ -\sqrt{2} \end{bmatrix}. \quad (6)$$

By applying (3) for the FSM and static mirror, the lateral position x_s and y_s of the laser spot on the sample in the x and y -direction can be calculated to

$$x_s = z_s \cdot \frac{\tan(\Delta\vartheta)}{\sin(\varphi + \Delta\varphi)} \quad (7a)$$

$$y_s = z_s \cdot \frac{1 - 2\cos^2(\Delta\vartheta)\cos^2(\varphi + \Delta\varphi)}{2\cos^2(\Delta\vartheta)\cos(\varphi + \Delta\varphi)\sin(\varphi + \Delta\varphi)}, \quad (7b)$$

with z_s the distance between sensor and sample in the object plane of the sensor. The measured distance z_{meas} and the distance z_s can be linked with the similarity theorems (see Fig. 4) in the following form

$$\frac{z_{\text{meas}} - z_{\text{lens}}}{y_{\text{lens}}} = \frac{z_s - z_{\text{lens}}}{y_{\text{lens}} - y_s}, \quad (8)$$

in which y_{lens} and z_{lens} are the position of the lens in the y and z -direction, respectively. By rearranging (7) and (8), the surface profile which is described by x_s , y_s and z_s can be calculated from the measured quantities in the following order

$$k_y = \frac{1 - 2\cos^2(\Delta\vartheta)\cos^2(\varphi + \Delta\varphi)}{2\cos^2(\Delta\vartheta)\cos(\varphi + \Delta\varphi)\sin(\varphi + \Delta\varphi)} \quad (9a)$$

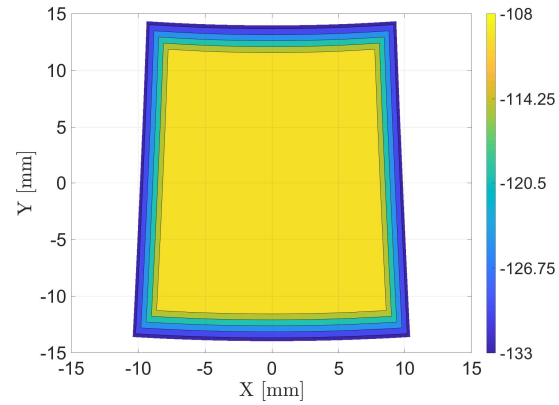


Figure 5: Obtainable lateral scan area of the scanning system. The lateral scan range increases towards the end of the measurement range.

$$z_s = \frac{z_{\text{meas}} \cdot y_{\text{lens}}}{y_{\text{lens}} + k_y \cdot (z_{\text{meas}} - z_{\text{lens}})} \quad (9b)$$

$$x_s = z_s \cdot \frac{\tan(\Delta\vartheta)}{\sin(\varphi + \Delta\varphi)} \quad (9c)$$

$$y_s = z_s \cdot k_y. \quad (9d)$$

The measurement range z_s of the laser line sensor is between 106 mm and 131 mm. Figure 5 shows the obtainable lateral scan area (calculated with (9)) for an actuation range of $\pm 3^\circ$. As can be observed, the lateral scan area increases towards the end of the measurement range, due to the tilted angle of incident. The lateral scan area is not squared, since both parameters x_s and y_s are dependent on both angular positions $\Delta\varphi$ and $\Delta\vartheta$. Furthermore, the obtainable area is not equal for the x and y -direction, which is caused by the orientation of the FSM ($\varphi = 45^\circ$). A lateral scan area of 15 x 23 mm can be observed over the entire measurement range. The maximum lateral resolution of the scanning system is determined by the laser spot diameter on the sample. The laser spot size on the sample is 60 μm in the center of the measurement range and expands to 250 μm towards the edges of the measurement range, due to divergence of the Gaussian beam. Adapting the focus of the laser, such that a smaller spot size (e.g. 30 μm) is achieved in center of the measurement range, would lead to a much larger spot size (e.g. 486.5 μm) at the edges of the measurement range. For a scanning system with a smaller measurement range, a smaller spot size and subsequent higher resolution can be achieved, since the length of the illumination path varies less between the center and edge of the measurement range. The angular resolution of the FSM (1 mdeg) has only a minor effect on the achievable lateral resolution, since the resulting position error (4.5 μm) is low as compared to the laser spot size. The resolution in the z -direction is mainly determined by the used laser line

Design and evaluation of an integrated scanning laser triangulation sensor

Table 1

Influence of a misalignment on the scan pattern.

Laser					
Parameter	x_L	y_L	z_L	φ_L	θ_L
Shift x [mm]	-0.1	0	0	0	-0.19
Shift y [mm]	0	-0.1	0	0.19	0
Std. dev. x [μm]	0	4.6	0	8.6	0.4
Std. dev. y [μm]	4.6	0.2	0	0.7	8.6
FSM					
Parameter	x_{FSM}	y_{FSM}	z_{FSM}	φ_{FSM}	θ_{FSM}
Shift x [mm]	0	0	0	0	0.24
Shift y [mm]	0	0.1	0.1	-0.34	0
Std. dev. x [μm]	0	0	0	7.8	7.8
Std. dev. y [μm]	4.6	6.6	0	1.3	11
Static mirror					
Parameter	x_{SM}	y_{SM}	z_{SM}	φ_{SM}	θ_{SM}
Shift x [mm]	0	0	0	0	-0.19
Shift y [mm]	0	-0.1	-0.1	0.27	0
Std. dev. x [μm]	0	4.6	4.6	1	15.5
Std. dev. y [μm]	0	6.6	6.6	1.3	11

sensor, which is 10 μm .

3.3. Effects of misalignment

Manufacturing tolerances and misalignment during the assembly strongly influence the achievable resolution of an optical measurement system [24]. To verify which parameters are vital during the alignment and to determine the required tolerances up front, a ray-tracing simulation is performed. For the simulation the position or orientation of the dot laser module, FSM and static mirror is modified by 0.1 mm or 0.1° from the reference position. Figure 6(a) depicts the effects of a misalignment on the scan pattern. As can be observed, a misalignment leads to a constant shift, which has no influence on the achievable resolution, and a distortion (see 6(b)) of the scan pattern. The lateral position of the laser spot on the sample is calculated using (9), such that a distortion of the scan pattern can not be obtained by the measurement system, which leads to an additional measurement error.

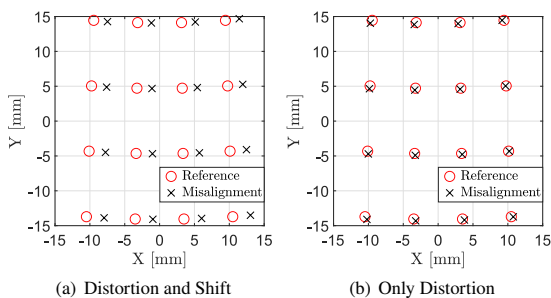


Figure 6: Simulated effects of a misalignment. The calculated scan pattern is (a) shifted and (b) distorted.

To characterize this error, initially the scan pattern is calculated with and without a misalignment. Subsequently the lateral shift, which minimizes the distance between the points from both calculations, is determined. This lateral shift is subtracted from the calculated scan pattern with misalignment. The resulting scan pattern is shown in Fig. 6(b). Finally, for each point the distance between the two corresponding points in the x and y -direction is calculated. Table 1 shows the resulting shift and standard deviation of the error for each component. As can be observed, the orientation and position of the static mirror strongly influences the achievable resolution, such that this component has to be aligned with particular attention. A misalignment of φ or θ can, however, be easily identified during the alignment, since this leads to a shift of the laser spot position during a movement between the start and end of the measurement range.

4. System hardware and scan trajectory

Figure 7 depicts the experimental setup of the scanning system. In order to align the various components according to the system design, the laser source is mounted on a post assembly and the remaining components are mounted on manual linear stages. To control the FSM a rapid prototyping system (Type: DS1202, dSPACE GmbH, Germany) with a sampling rate of 40 kHz is used. The measurement of the triangulation sensor is triggered by the dSpace platform, such that the measured distance is synchronized with the angular positions of the FSM.

4.1. Identification

To design tailored feedback controllers for the FSM, a model of each system axis is necessary. To derive this model, the system dynamics of the two system axes are measured with a system analyzer (type: 3562A, Hewlett-Packard, USA). The current through the coils serve as the

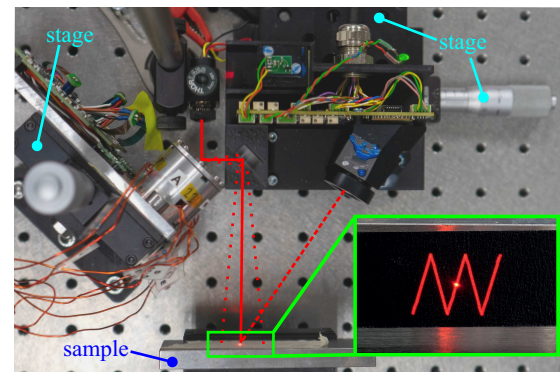


Figure 7: Experimental setup of the optical scanning system and long time exposure of a low resolution raster scan trajectory.

Design and evaluation of an integrated scanning laser triangulation sensor

system inputs, while the angular positions of the mirror are the system outputs (see [21]). For the identification the system analyzer uses a chirp signal (between 1 Hz and 10 kHz), with an amplitude of 100 mA [25].

Figure 8 depicts the measured frequency response of the tip (solid red) and tilt axis (solid magenta). Due to manufacturing tolerances the resonance frequency of the tilt axis is higher (415 Hz) as compared to the tip axis (315 Hz), such that separate models for each system axis are derived. Beyond the resonance frequency an increasing phase lag as well as a slope of -50 dB is observable for both system axes. This fractional order slope can be explained by eddy currents in the flux conducting parts of the actuator, which can be modelled by a lag-lead term [21]. At about 2 kHz the noise floor of the system is reached at about -60 dB. Figure 8 also shows the magnitude response of the cross-talk frequency responses (dashed dotted green and orange) between the two system axes. Since the magnitudes are about 16 dB lower as compared to the single axis transfer function (TF) over the relevant part of the frequency spectrum, each system axis can be controlled by a single-input-single-output (SISO) controller. According to [21] the dynamics of each system axis can be modelled by

$$P(s) = \underbrace{K \cdot \frac{\omega_0^2}{s^2 + 2\zeta_0\omega_0s + \omega_0^2}}_{\text{mass spring damper}} \cdot \underbrace{\frac{s + \omega_1}{s + \omega_2}}_{\text{eddy current}} \cdot \underbrace{e^{sT_d}}_{\text{time delay}}, \quad (10)$$

with the parameters according to Table 2, and DC gains of $K_{Tip} = 0.1663$ and $K_{Tilt} = 0.0935$ of the tip and tilt axis, respectively. The time delay of $T_d = 100\mu s$ is used to model

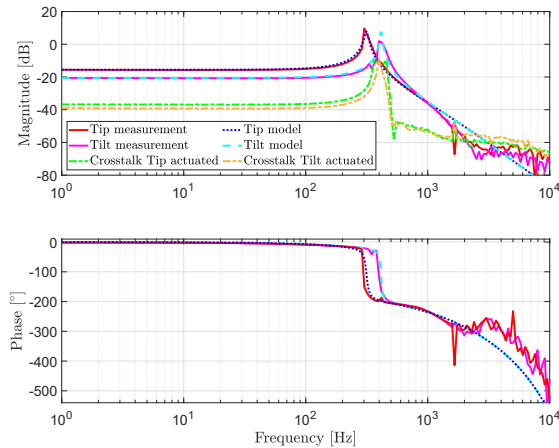


Figure 8: Measured and modelled frequency response of the tip and tilt axis. The resonance frequencies of the tip and tilt axis are at 315 Hz and 415 Hz, respectively. The measured crosstalk between the two axes is about 16 dB lower than the single axis response.

the entire delay from the current input to the sensor output including the phase lag of the dSpace platform and sensor system. The modelled TFs of the tip (dotted blue) and tilt axis (dashed cyan) are also shown in Fig. 8.

Table 2

Coefficients of the modelled FSM system axes.

Axis	Index	ω_{index} [rad/s]	ζ_{index}
Tip	0	1.98e3	0.033
Tilt	0	2.61e3	0.0187
Tip and Tilt	1	6.28e4	-
Tip and Tilt	2	1.26e4	-

4.2. Feedback Control

Based on the parametric nominal model feedback controllers are designed for the tip and tilt axis using an H_∞ -approach [26, 27]. The controllers are derived by minimizing the H-norm of the used extended model of a single axis. Figure 9 depicts this model, which consists of the controller C , identified system dynamic P and weighting functions W_S and W_U for the sensitivity function and input sensitivity function, respectively. Furthermore, the reference mirror position r , sensed position p , resulting error e , control effort u and measurement noise n are observable in the model. In order to guarantee a sufficient phase margin, the open loop crossover frequency is selected to 700 Hz. To enforce a good tracking within the selected bandwidth the requirements on the sensitivity function is formulated by the weighting function

$$W_S(s) = 0.1 \cdot \frac{s + z_{ws}}{s + p_{ws}}, \quad (11)$$

with the crossover frequency $z_{ws} = 2\pi \cdot 700$ Hz and $p_{ws} = 2\pi \cdot 0.01$ Hz. The weighting function W_S has a tamed inverse high pass behaviour, such that a good tracking at low frequencies is achieved [28]. In order to reduce the control effort at high frequencies the weighting function W_U of the input sensitivity function is selected to

$$W_U(s) = 0.0707 \cdot \frac{s + z_{wu}}{s + p_{wu}}, \quad (12)$$

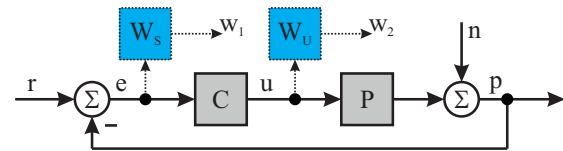


Figure 9: Block diagram of the extended model for the derivation of a feedback controller for one system axis. The weighting functions W_S and W_U for the sensitivity function and input sensitivity function are used to shape the controller C .

Design and evaluation of an integrated scanning laser triangulation sensor

with $z_{wu} = 2\pi \cdot 10$ kHz and $p_{wu} = 2\pi \cdot 100$ MHz. This leads to a low pass behaviour of the resulting system at higher frequencies. With the selected weighting functions and model of the two system axis, described in Section 4.1, the feedback controller of both axes can be derived to

$$C(s) = V \cdot \frac{\prod_{i=1}^3 s + \omega_{az_i}}{4} \cdot \frac{\prod_{i=1}^2 s^2 + 2\zeta_{bz_i} \omega_{bz_i} s + \omega_{bz_i}^2}{\prod_{i=1}^4 s + \omega_{ap_i}} \cdot \frac{\prod_{i=1}^2 s^2 + 2\zeta_{bp_i} \omega_{bp_i} s + \omega_{bp_i}^2}{2}, \quad (13)$$

with the coefficients according to Table 3, and the gain $V = 1.374e7$ and $V = 1.376e7$ for the tip and tilt axis, respectively.

The resulting TF of the controller (dotted green) of the tip axis is shown in Fig. 10. For low frequencies a high gain can be observed, such that a zero steady-state error is achieved. For a high phase margin at the selected crossover frequency, the phase of the controller increases between 100 Hz and 1 kHz. The measured open loop frequency response (dashed red) of the tip axis with the implemented controller is also depicted in Fig. 10. The crossover frequency of the system is 642 Hz. At this frequency a phase margin of 40° can be observed, the gain margin of the system is 10 dB, such that the open loop gain can additionally increase by a factor of three before the closed system goes unstable [29]. During operation only the stiffness of the FSM changes, which is further described in [21]. However, the crossover frequency of the open loop system is on the mass line, such that the changing dynamics do not influence the stability of the closed loop system, as the mass line is not affected by the change in stiffness (see [21]). At around 315 Hz a peak in the magnitude response is observable, which matches the resonance frequency of the tip axis. The control effort at this frequency is only slightly reduced by the controller.

Table 3

Coefficients of the controller for the tip and tilt axis.

Tip Axis				
Index	1	2	3	4
ω_{az_index} [rad/s]	1.26e4	1.26e5	6.28e8	-
ω_{ap_index} [rad/s]	0.033	6.3e4	4.82e5	9.49e6
ζ_{bz_index}	0.15	1	-	-
ω_{bz_index} [rad/s]	1.98e3	1.26e5	-	-
ζ_{bp_index}	0.87	0.56	-	-
ω_{bp_index} [rad/s]	2.39e4	4.68e5	-	-
Tilt Axis				
Index	1	2	3	4
ω_{az_index} [rad/s]	1.26e4	1.26e5	6.28e8	-
ω_{ap_index} [rad/s]	0.032	6.3e4	4.79e5	9.53e6
ζ_{bz_index}	0.2	1	-	-
ω_{bz_index} [rad/s]	2.61e3	1.26e5	-	-
ζ_{bp_index}	0.88	0.56	-	-
ω_{bp_index} [rad/s]	2.39e4	4.63e5	-	-

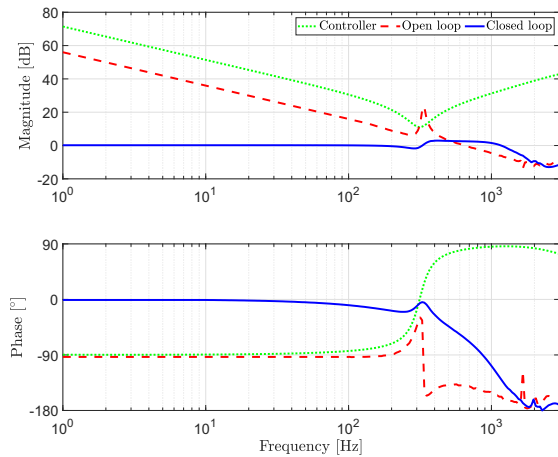


Figure 10: Measured controller TF (dotted green), loop gain (dashed red) and complementary sensitivity function (solid blue) of the tip axis. The crossover frequency of the open loop system is 642 Hz, with a phase margin of 40°.

Figure 10 also depicts the measured complementary sensitivity function (solid blue) of the system. Due to the low magnitude of the loop gain at around 300 Hz, the magnitude and phase of the complementary sensitivity function slightly decrease around this frequency. By selecting a higher crossover frequency, the magnitude of the loop gain could be increased, such that this decline could be avoided. Due to the high time delay of the sensor system (100 μ s), the crossover frequency can not be increased, without impairing the phase margin. The achieved -3 dB bandwidth of the tip axis is 1.4 kHz, the maximum peaking of 2.9 dB is reached at 400 Hz. For the tilt axis the same -3 dB bandwidth is achieved, with a slightly higher peaking (3.42 dB).

4.3. Scan Trajectory

Appropriate scan patterns are required to scan the area of interest on the sample. Raster trajectories are applied in various applications, like scanning electron microscopes [30], atomic force microscopes [31] and imaging systems [17]. A raster trajectory is generated by applying a slow triangular signal to one system axis and a fast triangular signal to the other axis. The resulting scan trajectory has a uniform scan speed and angular resolution [17].

However, a uniform spatial resolution (see Fig. 11(a)) is favoured for an imaging system. Since the geometrical relations are known (see (9)), the required reference signals for the fast and slow axis can be calculated up front. For the optical scanning system an image with 100 x 100 pixels is desired. Since the sample rate of the laser line sensor is 1 kHz, the scan speed of the fast reference signal is selected to 10 Hz. For the slow reference signal only the rising half of the trajectory is used to scan the sample (see Fig. 11(b)), such that the frequency needs to be 200 times smaller as

Design and evaluation of an integrated scanning laser triangulation sensor

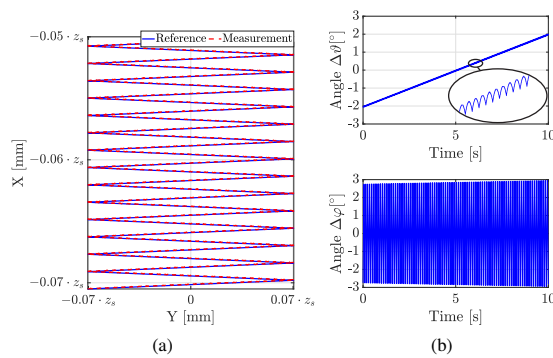


Figure 11: Raster trajectory. (a) demonstrates the dual axis operation with uniform spatial resolution. The lateral scan range depends on the distance z_s between sensor and sample. (b) depicts the reference signals for both system axes, which contain a fast and slow signal component, since both lateral positions depend on both angular positions.

compared to the fast signal. With the chosen frequencies of 10 Hz and 0.05 Hz, a framerate of 10 s can be achieved. It can be seen that the framerate is strongly determined by the sample rate of the applied laser line sensor. Since the compact FSM can be operated with the maximum actuation range of $\pm 3^\circ$ and a triangular signal up until 200 Hz, a framerate of 2 frames per second at a resolution of 100 x 100 pixels would be possible.

Figure 11(b) shows the reference signals for both system axes, which contain a fast and slow signal component. This is caused by the dependency between both lateral and angular positions (see (9)). The lateral resolution should be equal in the x and y-direction. The achievable scan range in the y-direction is, however, larger (see Fig. 5), such that the actuation range of $\Delta\theta$ is only $\pm 2^\circ$. As can be observed in Fig. 11(b), the actuation range of $\Delta\phi$ increases with the measurement time, which is also caused by the dependency between the angular and lateral position (see Fig. 5). Figure 11(a) demonstrates the dual axis operation, with the selected scan trajectory. As described in Section 3.2, the achievable lateral scan range depends on the distance between the sensor and sample, such that the in Fig. 11(a) shown lateral scan range is scaled by this distance. The actuation range of both axes of the FSM can be selected, such that large area scans as well as high resolution sectional scans can be performed.

5. Validation of the measurement results

To evaluate the performance of the scanning system the hollow cylinder shaped feature on a Duplo brick (type: Duplo Brick 2 x 4, Lego, Billund, Denmark), which is shown in Fig. 12(a), is measured. To validate the measurement results of the designed optical scanning system, reference measurements are acquired with a mechanical scanning triangulation sensor system, which is shown in Fig. 12(b). As

can be observed, this system consists out of two position controlled linear stages (type: VT-80 62309160, Physik Instrumente GmbH, Germany) and a laser triangulation sensor (type: ILD 2300-100, Micro-Epsilon GmbH, Germany).

Figure 12(c) depicts the measured surface profile of the optical scan, which features a similar shape to the in Fig. 12(a) shown sample. An incorrect value at $x = 5$ mm and $y = 0$ mm can be obtained in the surface profile, which is caused by multiple reflections at the edge of the cylinder. This type of artefact can be handled by inserting a threshold, which determines the valid height of the sample. In general the rough dimensions of the used sample are well known, since the measurement system is used to determine the deviations from the nominal dimensions. Along the y-axis the edges of the cylinder do not appear as steep as along the x-axis. This is caused by shading effects in the optical path of the laser sensor (see Fig. 4), such that certain areas on the sample can not be obtained. To reconstruct the surface profile, the missing measurement points are linear interpolated, which leads to the decreased slope along the y-axis. The surface beneath the cylinder shaped feature seems to be slightly bent at $y = -5$ mm (magenta circle), which is caused by a defocus of the reflected beam on the detector. As described earlier, the FSM is placed on the intersection line, such that the Scheimpflug condition is maintained. However, a rotation of the object plane also leads to a rotation

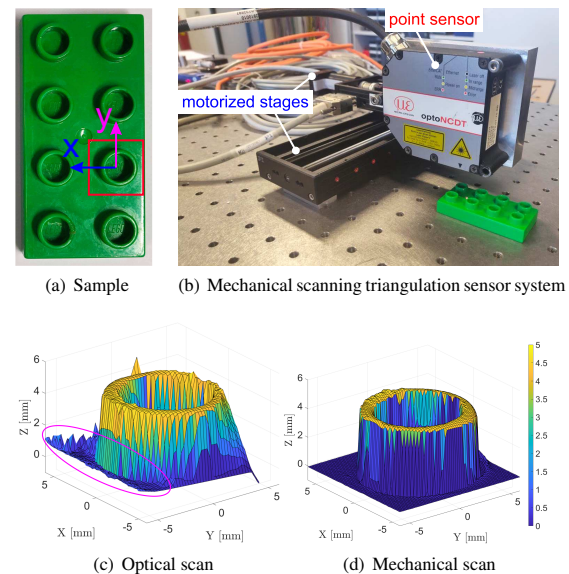


Figure 12: Measurement result. (a) shows the sample and selected area of interest. (b) depicts the mechanical scanning triangulation sensor system. (c) and (d) show the measured surface profile of the optical and mechanical scanning triangulation sensor system. In (c) the surface beneath the sample is slightly bent (magenta circle), which is caused by the fixed focal length of lens inside the triangulation sensor.

of the detector plane (see Fig 1(b)), since the focal length of the lens inside the triangulation sensor is fixed. The resulting error can be partially corrected by a correction polynomial, which was realized in [18], or by applying a varifocal lens. Figure 12(d) shows the measurement result of the mechanical scan. The edges can be detected more precisely with the mechanical scanning triangulation sensor system, due to the different sensor geometry (smaller angle of reflection) and the constant incidence angle of the illumination path.

To validate the achievable system performance of the optical scanning system the height of the hollow cylinder is determined. To calculate this height, only points which are on top of the feature should be used for the calculation. By applying a threshold for the height (80% of the maximum) points which are on the plane beneath the feature can be removed from the used data set. Artefacts caused by multiple reflection, would strongly influence the calculated height. Therefore, the height of the feature needs to be roughly determined in advance, which is realized by calculating the median value of the data set. The median value is hardly influenced by artefacts, such that this calculation method is more robust compared to a mean value calculation. Finally, for the data points which are within $\pm 1\%$ of the median value, the mean value and standard deviation is calculated. For the mechanical scan triangulation sensor system the height is determined to 4.493 mm with a standard deviation of $23.9\mu\text{m}$. This height is determined with the optical scanning system to 4.44 mm with a standard deviation of $24.5\mu\text{m}$, which agrees to the result of the mechanical scan. To capture a single point with the mechanical scanning triangulation sensor system takes 0.4 s, such that the measurement time to generate an image with 100×100 pixels is 67 minutes. To scan the sample with the same resolution takes only 10 s for the optical scan, such that the overall measurement time can be reduced by a factor of 400 compared to a mechanical scanning triangulation sensor system.

In summary the design of an integrated optical scanning triangulation sensor system is successfully validated, enabling comparable measurement results at a 400 times higher scan speed as compared to a mechanical scanning triangulation sensor system.

6. Conclusion and Outlook

This paper presents the development and evaluation of an integrated optical scanning laser triangulation sensor. To maintain the Scheimpflug condition, the FSM is placed on the intersection line of the lens and image plane. With the determined geometrical relations the surface of the sample can be reconstructed from the measured data. At the start of the measurement range a lateral scan area of 15×23 mm can be observed, which expands towards the end of the measurement range. Using ray-tracing simulations, the influence of misalignment on the achievable lateral resolution, which is $60\mu\text{m}$ at the maximum, is analyzed. Based on the identified system dynamics, feedback controllers for both system axes of the FSM are designed, using the H_∞ -approach,

which achieve closed loop bandwidths of 1.4 kHz. To scan the sample a scan trajectory, which generates a uniform spatial resolution, is applied, such that an image with 100×100 pixels is acquired in 10 s. To validate the system performance reference measurement with a classical mechanical scanning triangulation sensor system were performed. The measurement results show, that the calculated height of 4.44 mm and standard deviation of $24.5\mu\text{m}$ of the optical scan matches with the results of the reference measurement which is 4.493 mm and $23.9\mu\text{m}$. However, the measurement time can be reduced by a factor of 400 through the optical scan. Future work focuses on the correction of the error caused by the fixed focal length, as well as further system evaluation with resolution test targets.

Acknowledgment

The financial support by the Christian Doppler Research Association, the Austrian Federal Ministry for Digital and Economic Affairs, and the National Foundation for Research, Technology and Development, as well as MICRO-EPSILON MESSTECHNIK GmbH & Co. KG and ATENSOR Engineering and Technology Systems is gratefully acknowledged.

References

- [1] H. Kunzmann, T. Pfeifer, R. Schmitt, H. Schwenke, A. Weckenmann, Productive metrology - adding value to manufacture, CIRP Annals-Manufacturing Technology 54 (2005) 155–168.
- [2] R. Schmitt, F. Moenning, Ensure success with inline-metrology, in: XVIII IMEKO world congress Metrology for a Sustainable Development, 2006, pp. 235.1–235.6.
- [3] S. K. Everton, M. Hirsch, P. Stravroulakis, R. K. Leach, A. T. Clare, Review of in-situ process monitoring and in-situ metrology for metal additive manufacturing, Materials & Design 95 (2016) 431–445.
- [4] W. Gao, H. Haitjema, F. Fang, R. Leach, C. Cheung, E. Savio, J.-M. Linares, On-machine and in-process surface metrology for precision manufacturing, CIRP Annals 68 (2019) 843–866.
- [5] M. Grasso, B. M. Colosimo, Process defects and in situ monitoring methods in metal powder bed fusion: a review, Measurement Science and Technology 28 (2017) 044005.
- [6] T. Pfeifer, Koordinatenmeßtechnik für die Qualitätssicherung: Grundlagen-Technologien-Anwendungen-Erfahrungen, Springer-Verlag, 2013.
- [7] J. A. Sladek, Coordinate Metrology, Springer, 2016.
- [8] C. Yu, X. Chen, J. Xi, Modeling and calibration of a novel one-mirror galvanometric laser scanner, Sensors 17 (2017) 164.
- [9] R. Leach, Optical measurement of surface topography, volume 14, Springer, Berlin Heidelberg, 2011.
- [10] C. P. Keferstein, W. Dutschke, Fertigungsmesstechnik, Springer Vieweg, Wiesbaden, 2010.
- [11] K. Khoshelham, S. O. Elberink, Accuracy and resolution of kinect depth data for indoor mapping applications, Sensors 12 (2012) 1437–1454.
- [12] P. Zanuttigh, G. Marin, C. Dal Muto, F. Dominio, L. Minto, G. M. Cortelazzo, Time-of-flight and structured light depth cameras, Technology and Applications (2016).
- [13] F. J. Brosed, J. J. Aguilar, D. Guillomía, J. Santolaria, 3d geometrical inspection of complex geometry parts using a novel laser triangulation sensor and a robot, Sensors 11 (2010) 90–110.
- [14] A. Donges, R. Noll, Laser measurement technology, Springer, Atlanta, 2015.

Design and evaluation of an integrated scanning laser triangulation sensor

- [15] T. Yoshizawa, Handbook of optical metrology: Principles and Applications, CRC Press, 2017.
- [16] J. Schlarp, E. Csencsics, G. Schitter, Optical scanning of laser line sensors for 3D imaging, *Applied Optics* 57 (2018) 5242–5248.
- [17] J. Schlarp, E. Csencsics, G. Schitter, Optical scanning of a laser triangulation sensor for 3-d imaging, *IEEE Transactions on Instrumentation and Measurement* 69 (2020) 3606–3613.
- [18] J. Schlarp, E. Csencsics, G. Schitter, Influence of scheinpflug condition on measurements of a scanning laser line sensor for 3d imaging, *Journal of Physics: Conference Series* 1065 (2018) 142006.
- [19] J. Schlarp, E. Csencsics, G. Schitter, Scanning laser triangulation sensor geometry maintaining imaging condition, *IFAC-PapersOnLine* 52 (2019) 301–306.
- [20] J. Schlarp, E. Csencsics, G. Schitter, Sensoranordnung und Verfahren zum Vermessen eines Messobjekts, 2019. Deutsches Patent- und Markenamt 10 2019 200 664.7.
- [21] E. Csencsics, J. Schlarp, T. Schopf, G. Schitter, Compact high performance hybrid reluctance actuated fast steering mirror system, *Mechatronics* 62 (2019).
- [22] A. S. Householder, The theory of matrices in numerical analysis, Courier Corporation, 2013.
- [23] J. J. Craig, Introduction to robotics, Pearson Education India, 2009.
- [24] Y. Shimizu, R. Aihara, Z. Ren, Y.-L. Chen, S. Ito, W. Gao, Influences of misalignment errors of optical components in an orthogonal two-axis lloyd's mirror interferometer, *Optics express* 24 (2016) 27521–27535.
- [25] R. Isermann, M. Münchhof, Identification of dynamic systems: an introduction with applications, Springer Science & Business Media, 2010.
- [26] G. Schitter, A. Scarpas, F. Allgöwer, Robust two-degree-of-freedom control of an atomic force microscope, *Asian Journal of Control* 6 (2004) 156–163.
- [27] S. Skogestad, I. Postlethwaite, Multivariable feedback control: analysis and design, volume 2, Wiley New York, 2007.
- [28] E. Csencsics, G. Schitter, System design and control of a resonant fast steering mirror for lissajous-based scanning, *IEEE Transactions on Mechatronics* 22 (2017) 1963–1972.
- [29] R. Munnig Schmidt, G. Schitter, A. Rankers, J. van Eijk, The Design of High Performance Mechatronics – 2nd Revised Edition, IOS Press, Delft, 2014.
- [30] J. I. Goldstein, D. E. Newbury, J. R. Michael, N. W. Ritchie, J. H. J. Scott, D. C. Joy, Scanning electron microscopy and X-ray microanalysis, Springer, 2017.
- [31] A. Bazaie, Y. K. Yong, S. R. Moheimani, High-speed lissajous-scan atomic force microscopy: Scan pattern planning and control design issues, *Review of Scientific Instruments* 83 (2012) 063701.



J. Schlarp received an MSc. in Electrical Engineering from the Vienna University of Technology, Vienna, Austria in 2017 and is currently pursuing a PhD degree with the Automation and Control Institute (ACIN) of the Vienna University of Technology, Vienna, Austria.

His primary research interests are on high performance mechatronic systems and precision engineering for automated in-line metrology.



E. Csencsics is postdoctoral researcher in the Advanced Mechatronic Systems Lab at the Automation and Control Institute (ACIN) of TU Wien. He received an MSc. and a PhD degree (sub auspiciis) in Electrical Engineering from TU Vienna, Austria in 2014 and 2017, respectively.

His primary research interests are on high performance mechatronic systems, the development of holistic methods for multidisciplinary system design and integration, opto-mechatronic measurement and imaging systems, precision engineering, and robot-based inline measurement systems.

He received the journal best paper award of IEEE/ASME Transactions on Mechatronics (2018) and the best student paper award at the American Control Conference (2016).



G. Schitter is Professor for Advanced Mechatronic Systems at the Automation and Control Institute (ACIN) of TU Wien. He received an MSc in Electrical Engineering from TU Graz, Austria (2000) and an MSc and PhD degree from ETH Zurich, Switzerland (2004).

His primary research interests are on high-performance mechatronic systems, particularly for applications in the high-tech industry, scientific instrumentation, and mechatronic imaging systems, such as AFM, scanning laser and LIDAR systems, telescope systems, adaptive optics, and lithography systems for semiconductor industry. He received the journal best paper award of IEEE/ASME Transactions on Mechatronics (2018), of the IFAC Mechatronics (2008–2010), of the Asian Journal of Control (2004–2005), and the 2013 IFAC Mechatronics Young Researcher Award. He served as an Associate Editor for IFAC Mechatronics, Control Engineering Practice, and for the IEEE Transactions on Mechatronics.